

Phase coexistence and exchange-bias effect in LiMn_2O_4 nanorods

X. K. Zhang,* J. J. Yuan, Y. M. Xie, Y. Yu, F. G. Kuang, H. J. Yu, X. R. Zhu, and H. Shen

*School of Physics and Electronics, Gannan Normal University, Ganzhou 341000, China**and Institute of Optoelectronic Materials and Technology, Gannan Normal University, Ganzhou 341000, China*

(Received 3 September 2016; revised manuscript received 6 January 2018; published 5 March 2018)

In this paper, the magnetic properties of LiMn_2O_4 nanorods with an average diameter of ~ 100 nm and length of $\sim 1 \mu\text{m}$ are investigated. The temperature dependences of dc and ac susceptibility measurements show that LiMn_2O_4 nanorods experience multiple magnetic phase transitions upon cooling, i.e., paramagnetic (PM), antiferromagnetic (AFM), canted antiferromagnetic (CAFM), and cluster spin glass (SG). The coexistence between a long-range ordered AFM phase due to a Mn^{4+} - Mn^{3+} interaction and a cluster SG phase originating from frozen AFM clusters at low temperature in LiMn_2O_4 nanorods is elucidated. Field-cooled hysteresis loops (FC loops) and magnetic training effect (TE) measurements confirm the presence of an exchange-bias (EB) effect in LiMn_2O_4 nanorods below the Néel temperature ($T_N \sim 60$ K). Furthermore, by analyzing the TE, we conclude that the observed EB effect originates completely from an exchange coupling interaction at the interface between the AFM and cluster SG states. A phenomenological model based on phase coexistence is proposed to interpret the origin of the EB effect below 60 K in the present compound. In turn, the appearance of the EB effect further supports the coexistence of AFM order along with a cluster SG state in LiMn_2O_4 nanorods.

DOI: [10.1103/PhysRevB.97.104405](https://doi.org/10.1103/PhysRevB.97.104405)**I. INTRODUCTION**

Lithium manganese oxide, LiMn_2O_4 , as a promising candidate for a cathode material for application in rechargeable lithium-ion batteries (LIBs), has been extensively investigated due to its high operating voltage, high-energy density, low cost, and nontoxicity [1–7]. Apart from the technological importance, LiMn_2O_4 has also drawn considerable attention owing to its intriguing charge, orbital, and magnetic order [8–14]. However, up to now, there has been much controversy surrounding the magnetic structure of the ground state in LiMn_2O_4 . For example, Tomeno *et al.* have shown the presence of antiferromagnetic (AFM) long-range order in LiMn_2O_4 below the Néel temperature, $T_N = 65$ K, according to the observation of magnetic Bragg peaks [13]; Sugiyama *et al.* have also found a signature of AFM order below $T_N = 40$ K based on the Li nuclear magnetic resonance (^7Li -NMR) technique [15]. On the other hand, the absence of long-range magnetic order in LiMn_2O_4 at low temperature has also been reported by different research groups via neutron scattering measurements or electron spin resonance (ESR) spectroscopy [16,17]. Furthermore, a spin-glass (SG) behavior below 25 K was proved in LiMn_2O_4 through measurements of ac susceptibility and time-dependent remanent magnetization [11]. Interestingly, the coexistence of long-range order along with short-range order in LiMn_2O_4 has also been reported [9,12]. These discrepancies in the magnetic properties of LiMn_2O_4 probably come from chemical disorder (defects) and/or site disorder (Li/Mn) [9,17]. Therefore, in order to understand the nature of the magnetic properties of LiMn_2O_4 , a systematic characterization of stoichiometric samples is very crucial.

As we known, the magnetic properties of nanoparticles are usually dominated by the spins of the disordered surface shell due to an increase of the surface-to-volume ratio. Many experimental studies on AFM nanostructures have revealed various scenarios for the behaviors of surface spins, e.g., SG or cluster SG behavior, weak ferromagnetism, and diluted AFM in a field (DAFF) [18–22]. However, to the best of our knowledge, there are few reports on the magnetic properties of nanostructured LiMn_2O_4 especially in the one-dimensional (1D) case. In the present paper, we report the synthesis of 1D LiMn_2O_4 nanorods by a simple solid-state reaction and an investigation of their magnetic properties in detail. The dc and ac susceptibility measurements confirm the coexistence of an AFM ordered phase and a cluster SG phase in LiMn_2O_4 nanorods below ~ 60 K. Moreover, the exchange-bias (EB) effect in LiMn_2O_4 nanorods is verified by measurements of field-cooled hysteresis loops (FC loops) and the training effect (TE). By analyzing TE data, we can get to the conclusion that the observed EB effect originates from interface exchange coupling between the AFM and cluster SG states. In turn, the appearance of the EB effect also provides direct evidence of the phase coexistence of cluster SG and AFM long-range order at low temperature in LiMn_2O_4 nanorods. In addition, it should be noted that a shift in the FC loop has also been found in LiMn_2O_4 particles, and spatial segregation of AFM clusters and SG regions is suggested to explain the conflict between SG and long-range AFM order [11]. So, LiMn_2O_4 nanorods present similar magnetic behaviors with their corresponding bulk materials, which means that the nanodimensional effect or surface effect does not play a determinant role in the present compound.

II. EXPERIMENT

Single-crystalline LiMn_2O_4 nanorods were synthesized via a self-sacrifice template process. In brief, the precursor

*Author to whom correspondence should be addressed: zhangxianke77@163.com

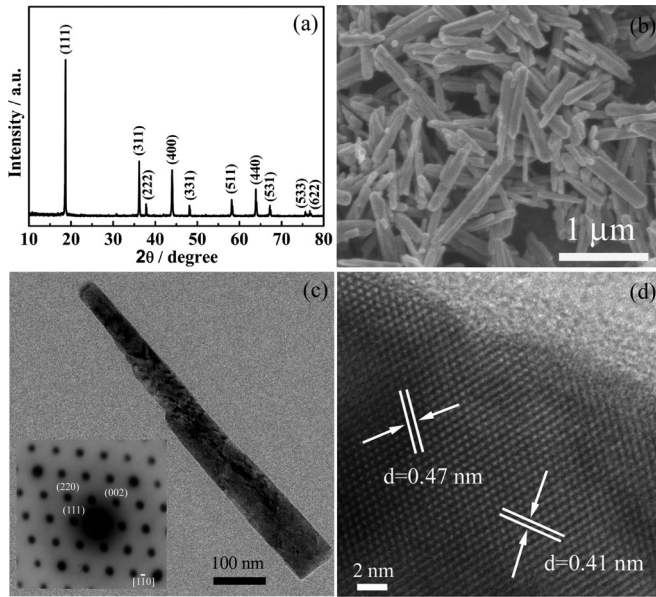


FIG. 1. (a) XRD pattern and (b) SEM image of as-synthesized LiMn_2O_4 nanorods. (c) TEM image of an individual LiMn_2O_4 nanorod and its SAED pattern (inset). (d) 2D HRTEM image.

β - MnO_2 nanorod templates were first prepared by a hydrothermal reaction as reported in a previous work [23]; then, LiMn_2O_4 nanorods were obtained through a simple solid-state reaction between β - MnO_2 nanorods and LiOH at 600°C in air for 12 h. The as-synthesized sample was characterized using an x-ray diffractometer (XRD, Rigaku, D/Max-RA) with $\text{Cu } K\alpha$ radiation ($\lambda = 1.54 \text{ \AA}$). The morphology and microstructures were investigated on a field emission scanning electron microscope (FE-SEM, JEOL JXA-8200) and a high-resolution transmission electron microscope (HRTEM, JEM-4000EX). The magnetic properties of the sample were measured using a commercial superconducting quantum interference device (SQUID) magnetometer [magnetic property measurement system (MPMS), Quantum Design]. For M - H measurements, the sample was cooled from 300 K to the required temperature under a cooling magnetic field (H_{cool}) and a zero field, and hysteresis curves were recorded thereafter under ± 50 kOe magnetic field. Furthermore, in order to minimize the trapped flux, the superconducting coils of MPMS were discharged from a high field (50 kOe) in the oscillation mode and the sample itself was also demagnetized in an oscillating field of decaying amplitude. The amount of remnant flux in the superconducting magnet was typically less than 10 Oe.

III. RESULTS AND DISCUSSION

Figure 1(a) shows a typical powder XRD pattern of the final product, which can be clearly indexed to a spinel structure of LiMn_2O_4 with the $Fd\bar{3}m$ space group (JCPDS card No. 35-0782). No impurity peaks were detected. A SEM image revealing the morphology of LiMn_2O_4 is presented in Fig. 1(b). It is evident that a large quantity of LiMn_2O_4 nanorods with an average diameter of ~ 100 nm and length of $\sim 1 \mu\text{m}$ has been obtained. A more detailed view of the morphology and microstructure of LiMn_2O_4 nanorods has been observed by

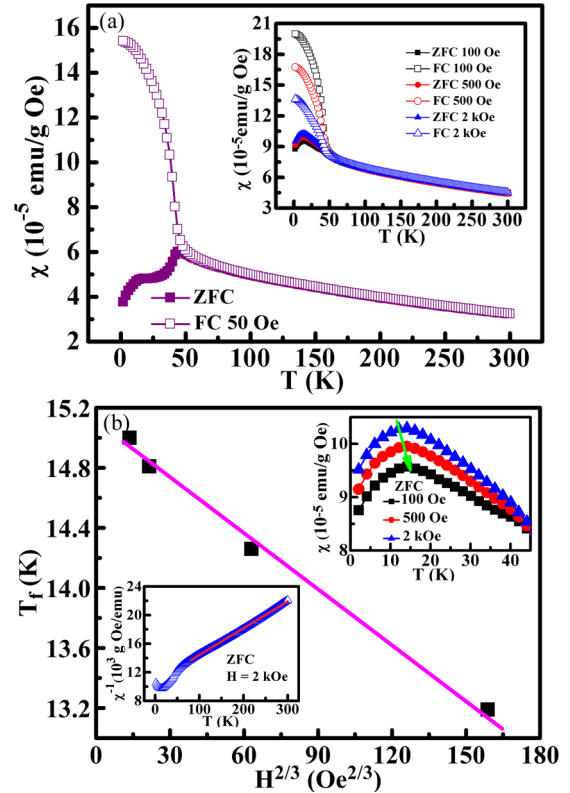


FIG. 2. (a) Temperature-dependent zero-field-cooled (ZFC) and field-cooled (FC) magnetization under an applied field of 50 Oe. The inset presents the temperature dependence of the magnetization measured in fields up to 2 kOe after ZFC (solid symbols) and FC (open symbols). (b) The peak temperature T_f as a function of $H^{2/3}$. The solid line represents a linear fit to Eq. (1). The upper inset shows the shift of T_f with the applied magnetic fields. The lower inset shows the inverse ZFC magnetic susceptibility. The solid line is a linear fit to Curie-Weiss law above 80 K.

means of a transmission electron microscope (TEM) combined with selected area electron diffraction (SAED). Figure 1(c) shows a TEM image of an individual LiMn_2O_4 nanorod. The SAED pattern along the $[1\bar{1}0]$ zone axis recorded from a single nanorod exhibits some bright spots [see the inset of Fig. 1(c)], indicating that the nanorod is single crystalline in nature. The diffraction spots can be indexed to the (220), (002), and (111) crystal planes of LiMn_2O_4 . Figure 1(d) is a two-dimensional (2D) HRTEM image, which further demonstrates the highly crystalline feature of the nanorod. The lattice spacings of 0.47 and 0.41 nm correspond to the (111) and (002) interplanar distances, respectively. On the basis of SAED and HRTEM, the growth direction of LiMn_2O_4 nanorods is determined to be their $[110]$ crystallographic orientation.

The magnetization susceptibility versus temperature curves $\chi(T)$ were taken in both zero-field-cooled (ZFC) and field-cooled (FC) modes. In Fig. 2(a) we show ZFC and FC data measured in a dc field of 50 Oe for LiMn_2O_4 nanorods, which presents three features, i.e., an irreversibility point at ~ 56 K, a sharp peak centered at ~ 45 K, and a flat peak at ~ 15 K. The splitting between the FC and ZFC curves below the irreversibility temperature ($T_{\text{irr}} \sim 56$ K) shows that the magnetic ordering temperature of LiMn_2O_4 nanorods is

higher than 56 K, which is in good agreement with previous reports [9,13,14,24]. In general, the AFM transition could be distinguished by a weak peak at the Néel point. While the weak peak is hardly observed on the present scale for LiMn₂O₄ nanorods, the nearly overlapped ZFC and FC curves over 60–300 K may indicate the existence of a long-range AFM order below 60 K. Interestingly, the ZFC curve shows a sharp peak at around 45 K, and the magnetization of the FC case is obviously larger than that of the ZFC case for $T < 45$ K, which may reveal the presence of a canted AFM order. Furthermore, it is also found that the proportion of the canted spin phase decreases and the transition at ~ 45 K is suppressed when applying a large magnetic field, as demonstrated in the inset of Fig. 2(a). It is obvious that the temperature-dependent behavior of the ZFC curve for 50 Oe is different from that for ZFC 100 Oe and for larger fields. Especially, the sharp peak observed at 45 K for 50 Oe data has decreased to be a weak anomaly with the increase of applied magnetic fields. These characteristics are consistent with a previous report [24]. So, the peak centered at $T = 45$ K in the ZFC curve and the steep increase of the FC curve suggest the appearance of a weak ferromagnetic state due to spin canting of the antiferromagnetically coupled manganese ions. Canted antiferromagnetism is usually caused by an antisymmetrical component of the superexchange interaction, i.e., the Dzyaloshinsky-Moriya (DM) interaction [25,26]. The transformation from a cubic to orthorhombic structure in LiMn₂O₄ at the Verwey temperature ($T_V = 290$ K) provides the necessary condition for the appearance of the DM interaction, since it vanishes by symmetry in a cubic $Fd\bar{3}m$ model. Based on the suggestion that the AFM order in LiMn₂O₄ originates from eightfold rings consisting of Mn⁴⁺ ions [14], we argue that Mn⁴⁺ ion spins do not lie exactly in the eightfold ring planes for $T \leq 45$ K, but are canted out of the planes by a small angle. This canting is driven by the rotation of MnO₆ octahedra in the orthorhombic phase which allows an antisymmetric superexchange term in the spin Hamiltonian. Therefore, the weak ferromagnetism in LiMn₂O₄ nanorods can be explained quite naturally as being due to the DM interaction.

Upon further cooling, the ZFC curve shows a flat peak at around 15 K where the peak position can be referred to as the freezing temperature (T_f), which indicates a SG or cluster SG behavior in LiMn₂O₄ nanorods. This behavior is consistent with previous reports [9,11]. For canonical SG systems, the irreversibility of magnetization occurs at a temperature close to but slightly below T_f [27]. Considering T_f is much lower than T_{irr} in the $M(T)$ curves, we think that LiMn₂O₄ nanorods most likely present a cluster SG state at low temperature. As we know, the peak T_f for a SG or cluster SG system usually shifts to the lower-temperature zone with an increase of the external magnetic field. The upper inset of Fig. 2(b) presents the low-temperature zone of $M(T)$ curves for the different applied fields. It can be seen that T_f shifts to a lower temperature with increasing magnetic field. Furthermore, the magnetic field dependence of the freezing temperature $T_f(H)$ can be described by the de Almeida–Thouless (AT) line [28]

$$H \propto [1 - T_f(H)/T_f(0)]^{3/2}, \quad (1)$$

where $T_f(0)$ is the freezing temperature for $H = 0$. The solid line in Fig. 2(b) presents the linear fit to the data with $T_f(0) = 15.09 \pm 0.06$ K. The conformance to the AT line

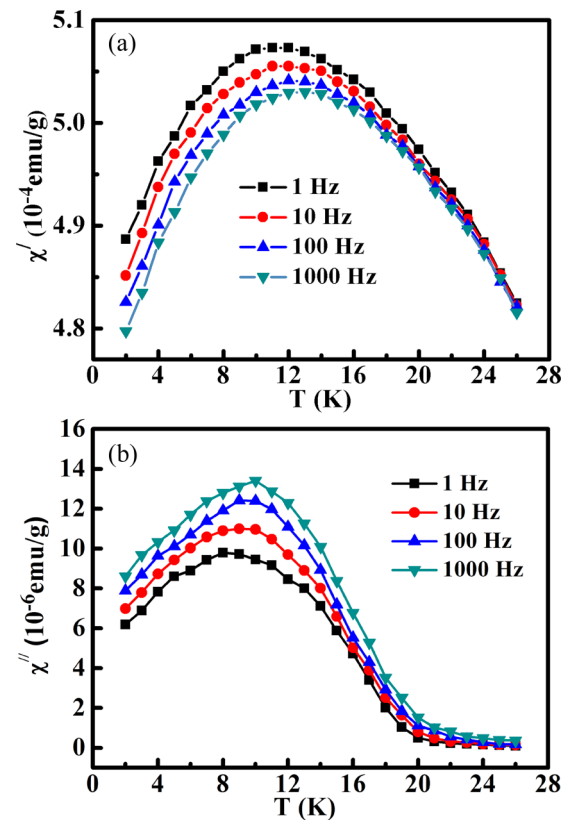


FIG. 3. (a) Temperature dependence of real part of ac susceptibility χ' at various frequencies. (b) Temperature dependence of imaginary part of ac susceptibility χ'' at various frequencies.

can be viewed as another hint for the presence of cluster SG behavior in LiMn₂O₄ nanorods. Now, turning towards the high-temperature region, the magnetization susceptibility of LiMn₂O₄ nanorods is found to follow the Curie-Weiss behavior $\chi = C/(T - \theta_W)$ above 80 K, which is demonstrated by a linear fit for the temperature dependence of the inverse susceptibility, as shown in the lower inset of Fig. 2. This fit yields an extrapolated Curie-Weiss temperature $\theta_W = -285$ K, revealing a dominant AFM exchange interaction between manganese ions in LiMn₂O₄ nanorods. The so-called frustration index $f = -\theta_W/T_N$ is found to be 4.8, which suggests that the system is moderately frustrated [29–31]. Moreover, the effective magnetic moment obtained from the high-temperature linear fit is $4.39\mu_B$, which indicates the Mn ions are considered to be a mixed valence state of Mn³⁺ ($t_{2g}^3 e_g^1$; $S = 2$; $4.90\mu_B$) and Mn⁴⁺ ($t_{2g}^3 e_g^0$; $S = 3/2$; $3.87\mu_B$), apparently in equal proportion. It should be noted here that the effective moment corresponds to the high spin state of Mn³⁺, which agrees with the result reported by Chowki and co-workers [9].

In order to confirm the appearance of cluster SG behavior, it is necessary to investigate the magnetically dynamic properties of LiMn₂O₄ nanorods at low temperatures. Figure 3(a) presents the temperature dependences of the real part (χ') of ac susceptibility with a probing field of 5 Oe. One can see that the peak position for each curve corresponding to a freezing temperature T_f shifts toward higher temperatures with an increase of frequency. Such a shift is not expected for usual

long-range ordered AFM or ferromagnetic (FM) systems. So, the behavior observed here is a typical characteristic of glassy systems. The value of the frequency sensitivity K has been used as a possible distinguishing factor for the presence of glassy phases, which is defined as [32,33]

$$K = \frac{\Delta T_f}{T_f \Delta \log \omega}. \quad (2)$$

The calculated K value is 0.044 for the current compound, which is larger than that of canonical SG systems such as CuMn (0.005) and AuMn (0.0045) but comparable to that of cluster SG systems [34–36]. So, the K value further verifies our system as a so-called cluster SG. Furthermore, Fig. 3(b) shows the imaginary part (χ'') of ac susceptibility as a function of temperature at various frequencies for LiMn₂O₄ nanorods. One observes that, as χ' , the frequency and temperature dependences of χ'' are similar to the behavior seen in SG systems.

A dynamical scaling analysis is performed by the conventional critical slowing down model of spin dynamics, which is given by the following relation [32,33],

$$\frac{\tau}{\tau_0} = \left[\frac{T_f - T_{SG}}{T_{SG}} \right]^{-z\nu}. \quad (3)$$

Here, T_f is the temperature of the maximum in χ' , and T_{SG} is the SG transition temperature; z is the dynamical exponent, and ν is the critical exponent of the correlation length ξ ($\xi = [(T_f - T_{SG})/T_{SG}]^{-\nu}$, and $\tau \propto \xi^z$); τ_0 is the characteristic time scale for spin dynamics; τ describes the dynamical fluctuation time scale and corresponds to the observation time at the temperature of maximum in χ' , and $\tau \propto 1/f$. Figure 4(a) presents $\log_{10}\tau$ plotted as a function of $\log_{10}[(T_f - T_{SG})/T_{SG}]$ with $T_{SG} = 10.45 \pm 0.05$ K obtained via the best fit to the power law given by Eq. (3), which shows a linear dependence as observed in most SG systems. The values of $\log_{10}\tau_0 = -6.72 \pm 0.03$ s ($\tau_0 \sim 1.9 \times 10^{-7}$ s) and $z\nu = 5.50 \pm 0.04$ are then obtained from the intercept and the slope yielded through a linear fit, respectively. For a typical SG system, $z\nu$ ranges from 4 to 12, and τ_0 lies between 10^{-11} and 10^{-13} s [33]. The value of $z\nu$ obtained from the present analysis is larger than the theoretically predicted value $z\nu = 4$ for the three-dimensional (3D) Ising model [37]. A similar low value of the critical exponent was reported in interacting magnetic nanoparticles with a dipole-dipole interaction [38] and interacting spin clusters [39]. However, the value of τ_0 (1.9×10^{-7} s) is somewhat larger than the typical single spin-flip times of conventional SG systems, which strongly implies that the SG state in the present LiMn₂O₄ nanorods is not atomic in origin but related to interacting atomic clusters. Further, the larger τ_0 value is normally observed in some FM or AFM cluster SG systems ($\tau_0 \sim 10^{-7}$ – 10^{-10} s) [35,40–42].

In addition, we also analyzed the transition near T_f in LiMn₂O₄ nanorods by means of the dynamic blocking of interacting clusters of spins. In this case, the phenomenological Vogel-Fulcher (VF) law can be used to investigate the frequency dependence of T_f , namely [43],

$$\tau = \tau_0 \exp \left[\frac{E_a}{k_B(T_f - T_{VF})} \right], \quad (4)$$

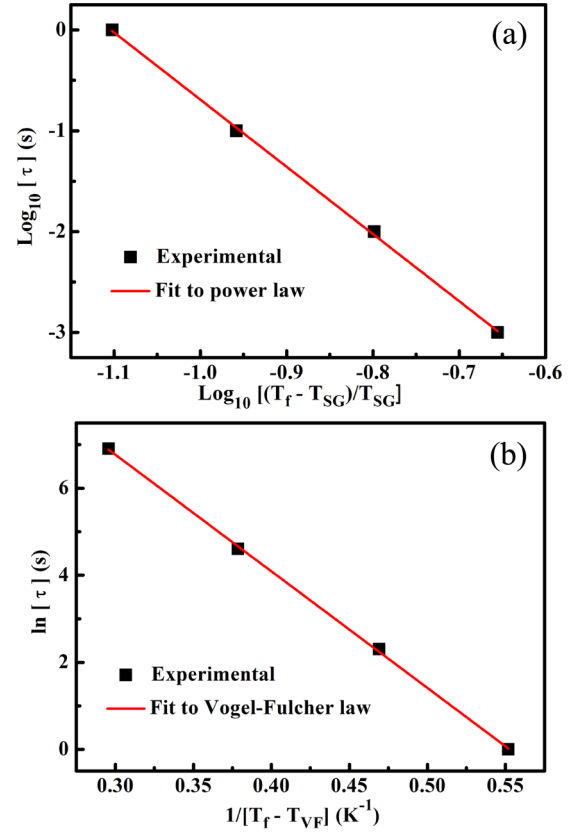


FIG. 4. (a) $\log_{10}\tau$ is plotted as a function of $\log_{10}[(T_f - T_{SG})/T_{SG}]$; the solid line is the fit to Eq. (3). (b) $\ln \tau$ is plotted as a function of $1/(T_f - T_{VF})$; the solid line is the fit to Eq. (4).

where E_a is the average thermal activation energy, k_B is the Boltzmann constant, T_f is the temperature of the maximum in χ' , and T_{VF} is the Vogel-Fulcher temperature, indicating a qualitative measure of the intercluster interaction strength. In Fig. 4(b), a plot of $\ln \tau$ vs $1/(T_f - T_{VF})$ is shown, which can be fitted well with the above VF model with $T_{VF} = 9.3$ K. A nonzero value of T_{VF} arises from the interaction between the spins and indicates the formation of spin clusters. The value of T_{VF} is smaller than T_{SG} from the power law [Eq. (3)] only by a few percent, in accordance with the general trend found in the cluster SG systems [41]. Having T_{VF} fixed, it is possible to obtain directly τ_0 and E_a/k_B from a linear fit to these data in the plot. The best fit, shown as the solid line in Fig. 4(b), yields the reasonable fitting parameters $\tau_0 = 3.7 \times 10^{-7}$ s and $E_a/k_B = 26.8$ K. The characteristic relaxation time obtained here is of the order of 10^{-7} s and is evidently larger than 10^{-13} s expected for the single atomic spins, which is consistent with the existence of magnetic spin clusters. In the frame of the VF model, $T_{VF} \ll E_a/k_B$ indicates a weak coupling regime and $T_{VF} \gg E_a/k_B$ means a strong one. T_{VF} is about $0.35 E_a/k_B$, which lies in the intermediate regime and confirms the presence of the interactions between magnetic entities in the present system. Moreover, the value of the parameter $\delta T_{Th} = (T_f - T_{VF})/T_f$ is proposed as a criterion for distinguishing between different universality classes [35,44]. The mean value of δT_{Th} is 0.21 for our compound, which is comparable

to values obtained for systems, described in terms of the progressive freezing of clusters, for example, $\text{La}_{0.5}\text{Sr}_{0.5}\text{CoO}_3$ [45]. Evidently, the VF law provides an excellent description of the experimental data, which suggests the SG behavior in LiMn_2O_4 nanorods can be attributed to the freezing of interacting magnetic spin clusters. A cluster SG is similar to a classical SG with the only difference being that the frozen entities in the cluster SG are not the individual spins but the magnetic moments (superspins) of collectives of atoms (nanoparticles).

Therefore, it is clear that both the power law and the VF law give an equally good fit for the real part data of ac susceptibility. Moreover, the difference in T_{VF} and T_{SG} is very small, and the τ_0 obtained using the power law has the same order of magnitude as that obtained using the VF law. Further, closer to T_{VF} (and T_{SG}), the VF law (the power law) can be adjusted to match the power law (the VF law) through the relation [46]

$$\ln(40k_B T_f / E_a) \sim \frac{25}{z\nu}. \quad (5)$$

With $T_f \sim 11.9$ K for $f = 100$ Hz, this relation gives $z\nu = 8.7$, which is larger than 5.5 obtained directly by a critical exponent analysis using the power law. However, according to the method used in Ref. [46], we can get another relation between the VF law and the power law for $f = 100$ Hz if the value of τ_0 decreases to 10^{-7} s,

$$\ln(23k_B T_f / E_a) \sim \frac{11.5}{z\nu}. \quad (6)$$

A value of $z\nu \sim 5.0$ can be attained with $T_f \sim 11.9$ K and $E_a/k_B = 26.8$ K via Eq. (6), which is close to 5.5 obtained using the power law. Thus, this further means the characteristic relaxation time in our compound is much larger than that of some typical SG systems.

The frequency dispersion exhibited by $\chi'(f, T)$ and $\chi''(f, T)$ for LiMn_2O_4 nanorods indicates a distribution of relaxation times associated with the dynamic characteristics of this magnetic system. To describe the relaxation of magnetic clusters in Mn-intercalated $\text{Ti}_{1+y}\text{S}_2$, Shand *et al.* obtained a linear model by assuming an exponential cluster sizes (volumes) distribution and $\omega\tau_c \ll 1$ [47],

$$\chi'' = -\left[\tan\left(\frac{n\pi}{2}\right)\right][\chi' - \Delta\chi]. \quad (7)$$

Here, $n = k_B T / E_0$, $E_0 = K V_0$, K is the anisotropy constant, and V_0 describes the width of the exponential size distribution. Note that $\Delta\chi$ is the difference between the isothermal and adiabatic susceptibilities. A fingerprinting method probing specifically the dynamic behavior of a system is the so-called Cole-Cole plot, which presents a graph of χ'' against χ' . A different shape of the $\chi''(\chi')$ curve has been obtained from the specific systems. The simplest plot is a semicircle ("Debye semicircle") signifying the presence of just one relaxation time in the system. However, the semicircle is flattened in SG, since it possesses a very wide distribution of relaxation times [33]. Figure 5 shows χ'' vs χ' plots at two different temperatures, one for $T > T_{SG}$ and the other for $T < T_{SG}$. It is obvious that excellent linear fits are obtained for the frequency range used, which indicates the good agreement between the experimental data and the model. This suggests that the relaxation time

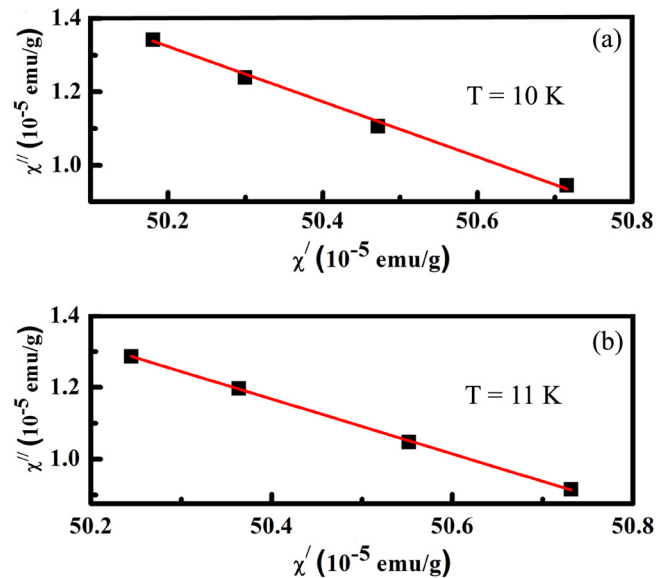


FIG. 5. χ'' vs χ' (Cole-Cole plot) for LiMn_2O_4 nanorods at (a) $T = 10$ K and (b) $T = 11$ K. Each data point corresponds to a specific frequency $1 \text{ Hz} \leq f \leq 1000 \text{ Hz}$. The linearity of the graphs is consistent with an exponential cluster-size distribution (see text).

behavior can be described well by an exponential distribution of magnetic cluster sizes in LiMn_2O_4 nanorods, which is similar to that of Mn-intercalated $\text{Ti}_{1+y}\text{S}_2$ with cluster spin-glass behavior [47]. Considering the differences in behavior between LiMn_2O_4 nanorods and more typical SG materials, we think that the exponential distribution of magnetic clusters seems to be the driving force for this departure from more conventional SG systems.

To further demonstrate the cluster SG behavior in the LiMn_2O_4 nanorods, we studied the magnetic relaxation. The following procedure was adopted to obtain thermal remanent magnetization (TRM) data. The sample was cooled under FC conditions with a 1 kOe field from the paramagnetic state (for example, 200 K) to a target temperature, and after stabilizing the temperature for a certain waiting time $t_w = 300$ s, the magnetic field was turned off. Subsequently, the magnetization (M) was recorded as a function of elapsed time (t). The relaxation of TRM was measured at four different temperatures: 2 K, where the spins are frozen, 10 K, which is just below the spin-glass freezing temperature T_f , and 20 and 40 K, which are above T_f . In Fig. 6, the normalized magnetization $m(t) = M(t)/M(0)$ is plotted as a function of time. In fact, a slow time decay of the magnetization was observed at all the temperatures below T_N , thereby establishing the glassy characteristic of magnetization. These data clearly suggest that the magnetic relaxation and glassy behavior are most prominent near the spin freezing temperature T_f . The decay curves can be well fitted by a stretched-exponential equation [9,29],

$$m(t) = m_0 - m_g \exp\left[-\left(\frac{t}{\tau}\right)^{1-n}\right], \quad (8)$$

where m_0 and m_g relate to the canted antiferromagnetism (weak ferromagnetism) and a glassy component mainly

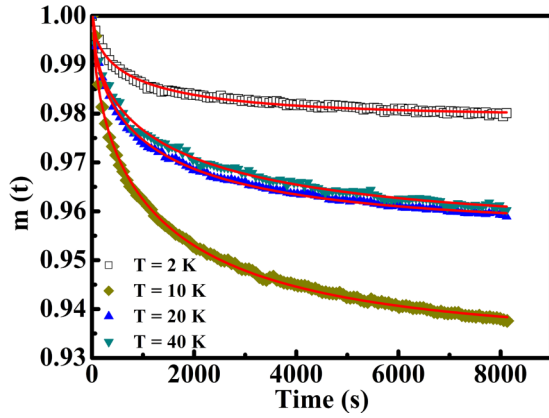


FIG. 6. Relaxation of normalized magnetization $m(t) = M(t)/M(0)$ at 2, 10, 20, and 40 K. Solid lines represent the stretched exponential fitting curves to Eq. (8).

contributing to the relaxation effects observed in LiMn_2O_4 nanorods, respectively. The time constant τ and the parameter n are related to the relaxation rate of the SG phase. The value of exponent n depends on the nature of energy barriers involved in the relaxation. For a SG system, n remains in the range $0 < n < 1$. The fitting parameter n was determined to be 0.47 at 20 K, 0.46 at 10 K, 0.47 at 20 K, and 0.50 at 40 K, respectively. Furthermore, we also measured the TRM data at 80 K, and no clear relaxation was observed. It should be noted that the existence of magnetic relaxation above T_f indicates the onset of frozen SG clusters below T_N .

On the basis of the above discussion, we argue that the long-range AFM order coexists with the cluster SG state in LiMn_2O_4 nanorods at low temperature. Next, we will present some explanations about the origin of the microscopic coexistence of AFM and cluster SG states. Rodriguez-Carvajal *et al.* proposed a charge-ordered pattern for LiMn_2O_4 , in which AFM-aligned Mn^{4+} ions form eightfold rings, and Mn^{3+} ions are situated in between the rings and inside of the rings [8]. Figure 7(a) presents a simplified projection of the proposed charge-ordered structure for LiMn_2O_4 along [001] orientation. Neglecting the z position of the atoms, it is obvious that the eightfold rings [black circles in Fig. 7(a)], containing all the Mn^{4+} , wrap two types of Mn^{3+} columns. One type is located in cubes consisting of four Mn^{3+} ions and four O^{2-} ions, which is at the center of eightfold rings of Mn^{4+} ions, and stacked along the c direction. The other type is situated in the spaces between neighboring eightfold rings, thus forming Mn^{3+} columns in the c direction. Gaddy *et al.* have indicated that the Mn^{4+} ions in the eightfold rings line up below $T_N \sim 66$ K, and these rings likely form the backbone of the long-range ordered AFM structure [14]. So, the observed AFM order in LiMn_2O_4 nanorods can be attributed to these eightfold rings in which the moments of Mn^{4+} ions become AFM aligned below $T_N \sim 60$ K. However, Mn^{4+} ion spins do not lie exactly in the eightfold ring planes for $T \leq 45$ K, but are canted out of the plane by a small angle, which gives rise to the weak ferromagnetism in LiMn_2O_4 nanorods.

On the other hand, if Mn vacancies or Li substitutions for Mn change the $\text{Mn}^{3+}/\text{Mn}^{4+}$ ratio in LiMn_2O_4 , one eightfold ring can interact with other rings via the intervening Mn^{3+}

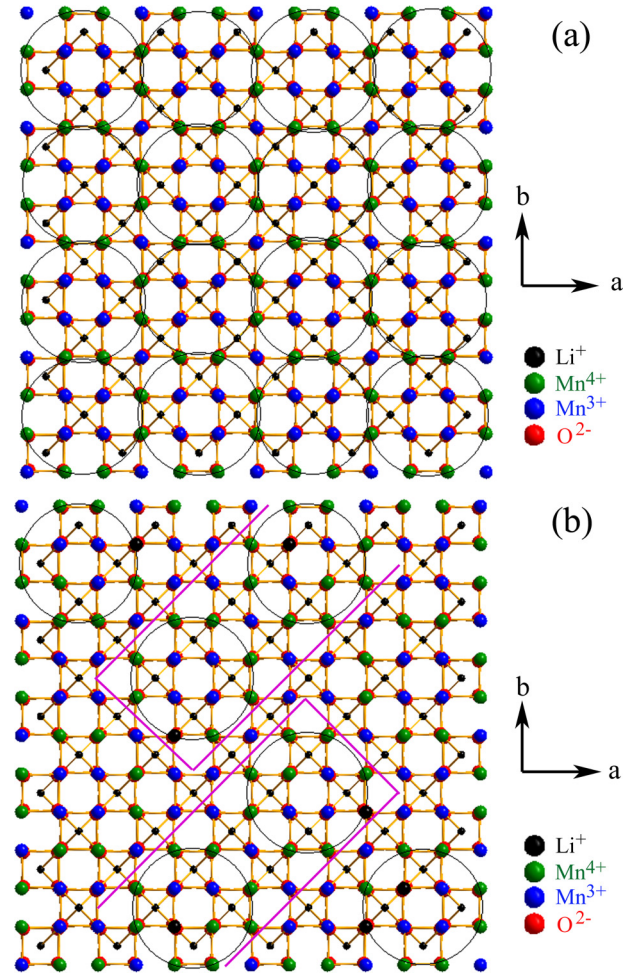


FIG. 7. Simplified projection of the charge-ordered pattern for LiMn_2O_4 . (a) AFM-aligned Mn^{4+} ions form eightfold rings (black circles), which act as the basic units of the long-range ordered AFM structure. (b) Mn vacancies or Li substitutions for Mn lead to modified rings and linked rings, some possibilities of which are presented. The solid lines (magenta) delineate large AFM clusters.

ions to act as large AFM clusters (superspins) [14]. Some possible large AFM clusters consisting of two eightfold rings are shown in Fig. 7(b). Furthermore, even much larger clusters can also form if the change of the $\text{Mn}^{3+}/\text{Mn}^{4+}$ ratio results in multiple rings being linked. As we know, it is very likely that there is a small fraction of oxygen vacancies or site disorder (Li at Mn site) in LiMn_2O_4 nanorods, which would lead to strongly couple the interaction between some octagonal cylinders and then to form large spin clusters. Therefore, structural defect (vacancies, substitutions) disorder resulting in a random exchange interaction between manganese ions should be responsible for the observed cluster SG behavior in LiMn_2O_4 nanorods. Furthermore, AFM interactions between Mn ions located on octahedrally coordinated sites in LiMn_2O_4 are expected to be geometrically frustrated; inelastic neutron scattering experiments have shown that $\text{Mn}^{4+} - \text{Mn}^{4+}$ spin fluctuations present a critical slowing down, and freeze out below around 25 K, while $\text{Mn}^{3+} - \text{Mn}^{3+}$ spin fluctuations persist at least down to 4 K [48]. Thus, the cluster SG behavior observed here should be attributed to the freezing of AFM

superspins due to the slow dynamics of Mn^{4+} . So, both the long-range AFM order and the cluster SG dynamics in LiMn_2O_4 nanorods are associated with the same Mn^{4+} entity on the basis of eightfold rings. However, the contribution of a small fraction of Mn^{3+} to AFM order and the cluster SG state cannot be ruled out. The coexistence between AFM long-range order and SG phase has also been observed in the dilute Ising systems $\text{Fe}_{0.55}\text{Mg}_{0.45}\text{Cl}_2$ [49] and $\text{Fe}_{0.6}\text{Mn}_{0.4}\text{TiO}_3$ [50], quantum Heisenberg antiferromagnets $\text{Cu}_2(\text{OH})_3(\text{C}_m\text{H}_{2m+1}\text{COO})$ [30], as well as multiferroic $\text{PbFe}_{0.5}\text{Nb}_{0.5}\text{O}_3$ [51,52].

As we know, an exchange interaction at the interface between a FM and an AFM spin structures is expected to result in the EB effect, which has attracted significant interest during the past 50 years due to its intriguing physics as well as technological applications [53,54]. In general, the EB effect manifests itself as a shift of the center of a magnetic hysteresis loop from the origin when a FM/AFM system is cooled in a static magnetic field through T_N of the AFM system. Besides FM/AFM interfaces, the EB effect has also been observed in other types of interfaces such as ferrimagnet (FI)/AFM, FI/FM, FM/SG, AFM/SG, and FI/SG [53,54]. Since LiMn_2O_4 nanorods show the coexistence of AFM and cluster SG states at low temperature, it would be interesting to explore if the EB effect could appear in this phase-coexisting system. In order to check for the possibility, field-cooled hysteresis loops (FC loops) were measured. Figure 8(a) shows the magnetic hysteresis loops measured between ± 50 kOe after cooling the sample from room temperature to 2 K under both ZFC and FC conditions with a magnetic field of 2 kOe. These M - H curves keep a nearly linear slope in the field range used except the central zone, which is usually considered from an AFM system. An enlarged view of the central part of the M - H curves is presented in the inset of Fig. 8(a), which shows the ZFC hysteresis loop keeps a good central symmetry about the origin, whereas the FC loop is strongly displaced from the origin and broadened along the applied field direction, namely, the EB effect.

It should be noted that the observed FC loop here is unsaturated within a maximal field of 50 kOe, which seems that the M - H loop may be due to a minor loop effect. However, the minor loop is nonsymmetrical and is expected to present significant vertical asymmetry as well. The equal magnetization values at the highest positive and negative magnetic fields, as shown in Fig. 8(a), may indicate that the shifted hysteresis loop in LiMn_2O_4 nanorods is the conventional EB effect [55–57]. Moreover, materials involving disordered magnetic and/or glassy magnetic phases or canted spin configuration or systems with large anisotropy do not show a saturating trend [56,58]. In order to further verify the appearance of the EB effect in our compound, we measured M - H loops between ± 50 kOe at $T = 2$ K after cooling with ± 5 kOe bias field ($H_{\text{cool}} = \pm 5$ kOe). The region near the origin is blown up to present the extent of EB clearly, as shown in Fig. 8(b). The shape of the full loop remains the same as the shape in the case of the ZFC loop. The EB effect observed in this case is conventional as the measurement has been carried out after field cooling under $+5$ and -5 kOe and the path followed in tracing the loop is as follows: $+5$ kOe $\rightarrow 0 \rightarrow -50$ kOe $\rightarrow 0 \rightarrow +50$ kOe. It is evident that cooling under a positive (negative) field yields a hysteresis loop shift in a negative

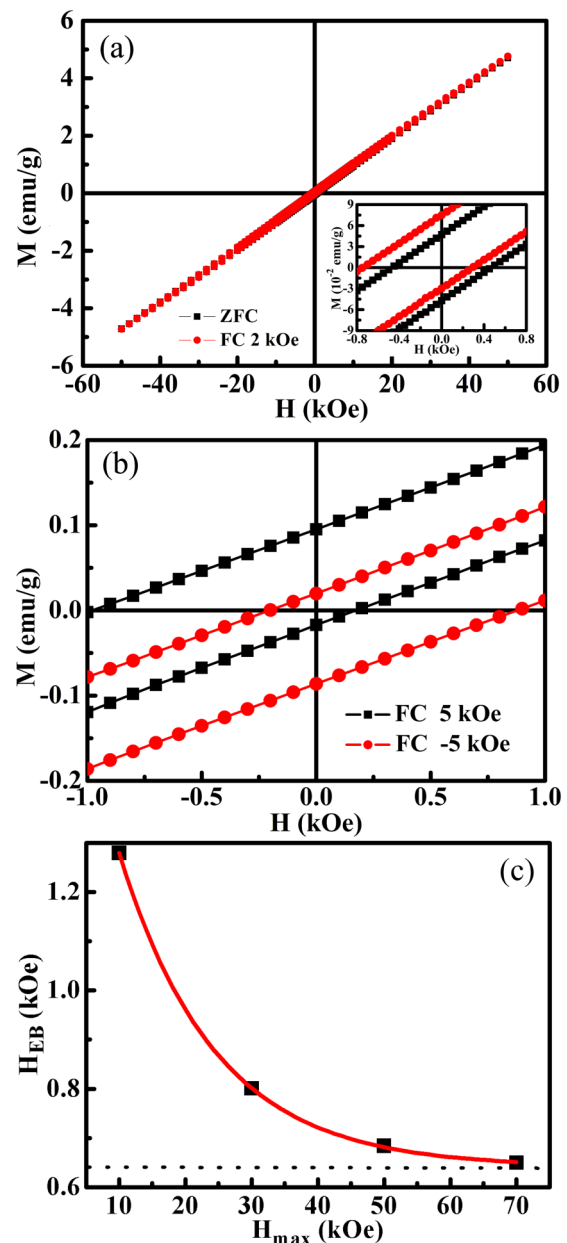


FIG. 8. (a) M - H loops under ZFC and FC conditions measured at 2 K. The inset is the central part of the M - H loops clearly showing a shift of the FC loop along the field axis. (b) Central parts of M - H loops measured at 2 K after cooling with the opposite magnetic fields of ± 5 kOe, which shows the reversible shift of the hysteresis loop. (c) H_{EB} as a function of the maximum field of the loop (H_{max}) measured at 2 K with $H_{\text{cool}} = 10$ kOe, where $H_{\text{max}} = 10, 30, 50,$ and 70 kOe. The solid line denotes the best fit to Eq. (9), and the dotted line indicates the asymptotic value $H_{\text{EB}}(\infty)$ which is the intrinsic H_{EB} .

(positive) direction along the field axis. The EB field (H_{EB}) is generally defined as $H_{\text{EB}} = -(H_1 + H_2)/2$, where H_1 and H_2 are the left and the right coercive fields, respectively. The values of EB for both positive and negative bias fields are 404 and -337 Oe, respectively. Furthermore, the H_{EB} observed here for the positive (negative) cooling field is asymmetric, which may be caused by the local spin texture at the interface between the AFM and cluster SG states which generates a nonswitchable

unidirectional anisotropy along the negative direction of the applied field [22,55]. So, the shift of hysteresis loop in the negative and positive directions of the field axis can be reversed by applying an opposite cooling field, as in the case of various EB systems. This further supports the presence of an EB effect in the present system, which also indicates the coexistence of ordered AFM and cluster SG states at low temperatures [18,29,59].

Furthermore, it was suggested that the existence of a “true” EB effect in nonsaturating systems may be verified by “effectively saturated” hysteresis loops where the ascending and descending branches of the loop coincide at fields higher than the anisotropy field [60,61]. The appropriate value of the maximum field of the loop (H_{\max}), at which the minor loop effect is sufficiently small, can be estimated by measuring H_{EB} as a function of H_{\max} at constant parameters of temperature and cooling field. As shown in Fig. 8(c), H_{EB} vs H_{\max} dependence measured at 2 K under a 10 kOe cooling magnetic field is presented. One can find that the dependence curve can be well fitted by an exponential equation [62],

$$H_{\text{EB}} = H_{\text{EB}}(\infty) + H_0 \exp(-\alpha H_{\max}). \quad (9)$$

In this equation, $H_{\text{EB}}(\infty)$ is the limit value of the EB field when $H_{\max} \rightarrow \infty$, and H_0 and α are the fitting parameters. The best fit presents $H_{\text{EB}}(\infty) = 641$ Oe. This procedure shows that the H_{EB} measured with $H_{\max} = 50$ kOe differs by $\sim 6\%$ only from the true value of H_{EB} , i.e., the asymptotic value of H_{EB} ($H_{\max} \rightarrow \infty$). So, we believe that, in such circumstances, although it is hard to rule out the contribution of a minor loop effect since complete saturation is not technically obtained, the experimental results support the existence of the EB effect in LiMn_2O_4 nanorods. Much more sensitive experimental tools such as polarized neutron reflectometry (PNR) and x-ray magnetic circular dichroism (XMCD) may allow us to determine whether a shift of the magnetization curve for the unpinned component is due to exchange anisotropy or an artifact of the measurement (i.e., a minor loop) [58,63].

Further insight into the evolution of the EB effect in LiMn_2O_4 nanorods is obtained from the dependence of hysteresis loops on the cooling field (H_{cool}). Figure 9(a) presents the FC loops measured with different cooling fields at 2 K. The inset of Fig. 9(a) shows an enlarged view of the central region of the FC loops, which reveals the obvious shifts of the hysteresis loops toward the negative magnetic fields. Figure 9(b) shows that the magnitude of H_{EB} increases with increasing H_{cool} and then shows a tendency to saturation. A similar cooling field dependence of H_{EB} was observed in core-shell-type $\text{BiFe}_{0.8}\text{Mn}_{0.2}\text{O}_3$ nanoparticles [64] and polycrystalline $\text{Sr}_2\text{LuRuO}_6$ samples [65]. With the increase of the cooling field, more and more frozen-in spins are created, which leads to changes in the magnetic configuration at the AFM/SG interface. Therefore, H_{EB} increases with an increase of the cooling field. In turn, the strong dependence of the cooling field on the exchange-bias magnitude is another fingerprint for the existence of a SG phase in the present compound.

Figure 10(a) presents the FC loops measured after cooling in a magnetic field $H_{\text{cool}} = 10$ kOe with the maximal field $H_{\max} = 50$ kOe across 2–80 K. The inset of Fig. 10(a) shows an enlarged view of the central region of the FC loops measured at different temperatures, which reveals obvious shifts of

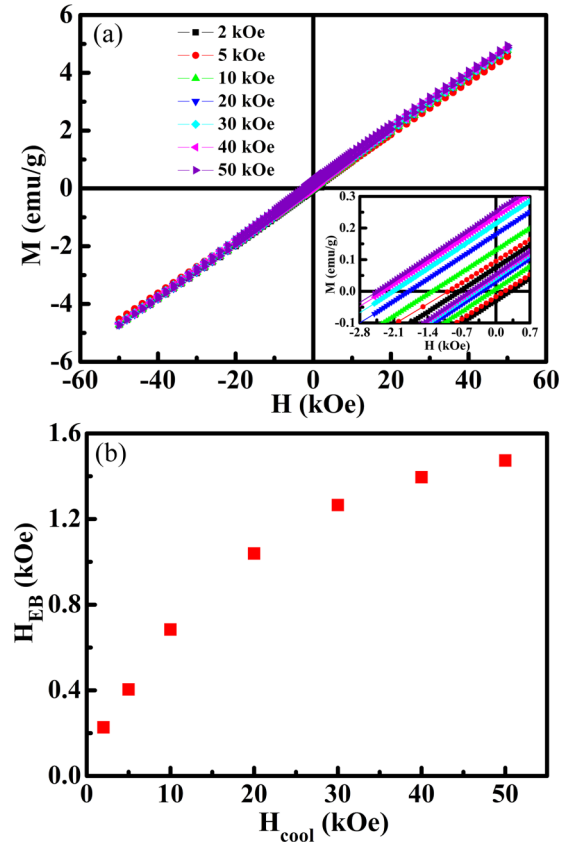


FIG. 9. (a) FC loops measured at 2 K under different cooling fields $H_{\text{cool}} = 2, 5, 10, 20, 30, 40,$ and 50 kOe. The inset shows the central part of these loops, which presents the clear shift of M - H curves. (b) H_{EB} as a function of the cooling field.

the hysteresis loops toward negative magnetic fields below ~ 60 K. Figure 10(b) illustrates the temperature evolution of H_{EB} , which shows that H_{EB} decreases sharply with increasing temperature and almost vanishes at ~ 60 K, in correspondence with the Néel temperature T_N , not the freezing temperature T_f . It is important to note that hysteresis loops are observed at all temperatures below T_N , which indicates that the freezing of the cluster SG occurs simultaneously with the onset of AFM order and finally completes below T_f after a progressive freezing process. The existence of spin frustration is known to result in an exponential temperature-dependent decay of $H_{\text{EB}}(T)$, which can be expressed as [59,66–68]

$$H_{\text{EB}}(T) = H_{\text{EB}}(0) \exp\left(-\frac{T}{T_1}\right), \quad (10)$$

where $H_{\text{EB}}(0)$ is the extrapolation of $H_{\text{EB}}(T)$ at $T = 0$ K; T_1 is a constant, indicating the temperature that $H_{\text{EB}}(0)$ drops to $1/e$ of its initial value. The best-fitting parameters are $H_{\text{EB}}(0) = 812.5$ Oe and $T_1 = 10.4$ K. The good fit to Eq. (10) gives an obvious indication for the scenario that the EB effect is strongly related to the cluster SG state in LiMn_2O_4 nanorods. Such an exponential decay of H_{EB} with temperature has been observed in a range of diverse materials related to magnetically frustrated systems in which the competing magnetic domains form a SG state [59,68–70].

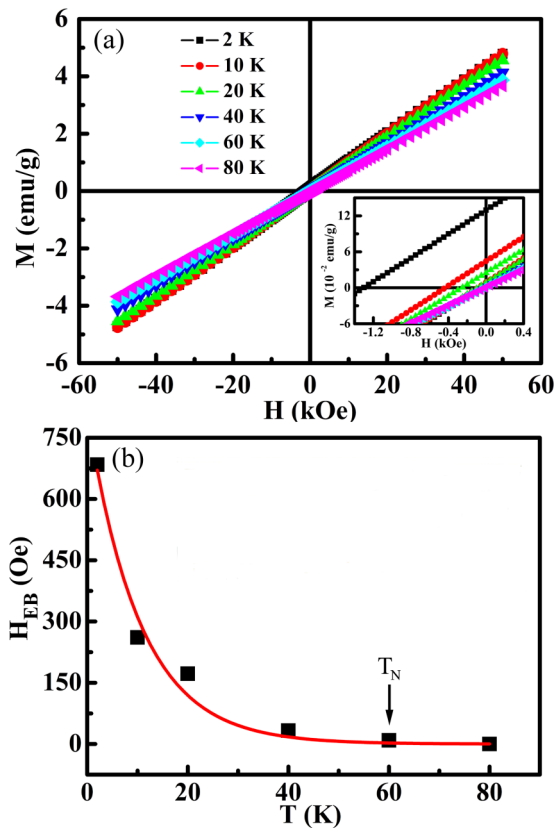


FIG. 10. (a) FC loops measured at different temperatures after cooling in a magnetic field $H_{\text{cool}} = 10$ kOe with the maximal field $H_{\text{max}} = 50$ kOe. The enlarged central part of the FC loops showing the presence of the EB effect. (b) Temperature dependence of H_{EB} for LiMn_2O_4 nanorods. The solid line presents the fit to Eq. (10). The arrow marks the Néel temperature (T_N) of LiMn_2O_4 nanorods.

Another important characteristic of an EB system is the existence of the so-called training effect (TE), which manifests itself by the reduction of H_{EB} with the number of consecutive hysteresis loops (n) at a constant temperature. In order to elucidate the origin of the EB effect in LiMn_2O_4 nanorods, we continuously measured several consecutive hysteresis loops as well. Figure 11(a) shows the portion of M - H loops near the origin under field cooling with a 10 kOe magnetic field at 2 K, while the actual measurements took place between -50 and 50 kOe. Usually, the shift of the consecutive hysteresis loops is most pronounced at the left branch of a loop, while the right branch only slightly shifts. It is very obvious that the magnetic TE is presented in our sample, as shown in Fig. 11(b). A significant reduction of H_{EB} was observed between the first and the second loops where it falls by $\sim 15\%$ and then it gradually decreases with increasing n . An empirical power law suggested by Pacard *et al.* for fitting H_{EB} as a function of n ($n > 1$) has been widely used to describe TE [71],

$$H_{\text{EB}}(n) - H_{\text{EB}}(\infty) = \frac{k}{\sqrt{n}}, \quad (11)$$

where k is a material-dependent constant; $H_{\text{EB}}(n)$ and $H_{\text{EB}}(\infty)$ are magnitudes of the EB field for the n th cycle and in the limit of infinite loops, respectively. The solid line (blue color) in Fig. 11(b) shows the best-fitting curve of experimental data

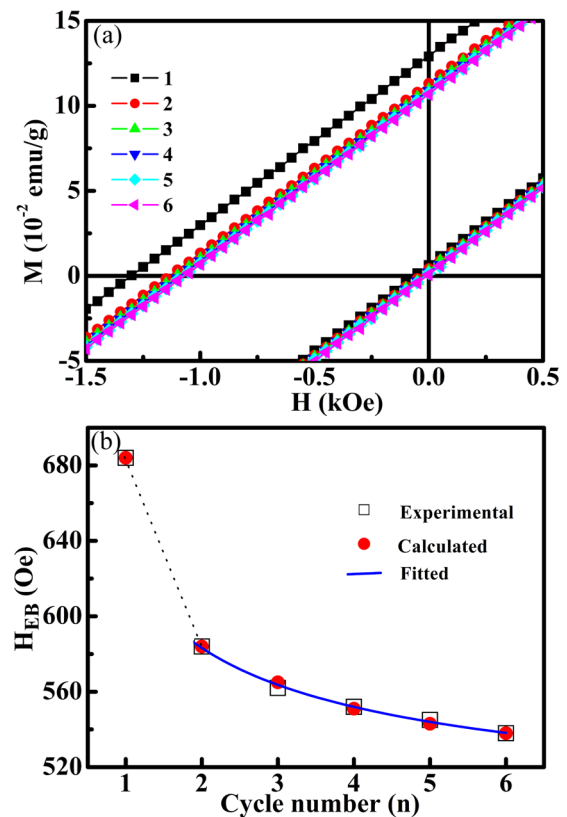


FIG. 11. (a) The enlarged view of consecutively measured hysteresis loops after cooling in a field of 10 kOe to reveal the shift of the loops with increasing loop number (n). (b) The EB field (H_{EB}) dependence on the number of field cycles (n). The open squares (black) are the experimental data. The solid circles (red) represent the calculated data points using Binek's recursive formula. The solid line (blue) represents the best fit to Eq. (11) for $n > 1$. The dotted line (black) joining the data is only a guide to eyes.

for H_{EB} for $n > 1$ using Eq. (11). The resulting parameters are $H_{\text{EB}}(\infty) = 477$ Oe and $k = 151$ Oe. The fit clearly shows a good agreement with the data for $n > 1$. It should be noted that the experimental value for $n = 1$ ($H_{\text{EB}} = 684$ Oe) significantly exceeds the value obtained by Eq. (11) for $n = 1$ ($H_{\text{EB}} = 628$ Oe), which further shows this law holds only for $n > 1$. The strong and significant decrease of H_{EB} between the first and the second hysteresis cycles may suggest some initial nonequilibrium arrangement or metastable state of the AFM domains [72–74].

Considering TE in the thermodynamic framework of spin configurational relaxation at the AFM surface, Binek proposed a recursive formula for TE [75],

$$H_{\text{EB}}(n+1) = H_{\text{EB}}(n) - \gamma [H_{\text{EB}}(n) - H_{\text{EB}}(\infty)]^3. \quad (12)$$

Here, $H_{\text{EB}}(n)$ and $H_{\text{EB}}(\infty)$ are magnitudes of the EB field for the n th cycle and in the limit of infinite loops, respectively; γ is a system-dependent constant. The best-fit curve of the experimental data with Eq. (12) yields the fitting parameters $H_{\text{EB}}(\infty) = 447$ Oe and $\gamma = 7.5 \times 10^{-6}$ Oe⁻². Taking the respective initial value ($n = 1$) of H_{EB} as obtained from the experiment, the theoretical data [$n \geq 2$, solid circles in Fig. 11(b)] are calculated from the recursive formula in Eq. (12)

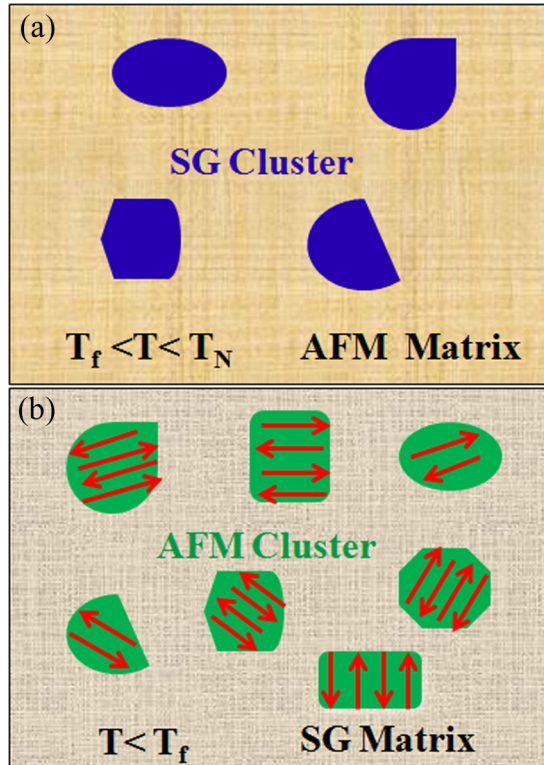


FIG. 12. A phenomenological model revealing the origin of the EB effect in LiMn₂O₄ nanorods. (a) SG clusters (blue) are embedded in an AFM matrix for $T_f < T < T_N$. (b) AFM clusters (green) are embedded in a SG matrix for $T < T_f$.

by using the obtained fitting parameters [59,64,74,76]. It is remarkable that the theoretical results are consistent with the experimental results not only for $n > 1$ but also for $n = 1$. Clearly, Eq. (12) describes the TE of the EB effect fairly well, not only for $n > 1$ but also for $n = 1$. Therefore, the TE in LiMn₂O₄ nanorods can be described successfully by Binek's model. This model has been used successfully to fit the TE data of a wide variety of systems such as FM/AFM bilayers, FM hard/FM soft bilayers, spontaneously phase-separated systems, FM nanodomains embedded in an AFM matrix, and core-shell nanoparticles, where interface exchange coupling was the only origin of the EB phenomenon [64]. On the basis of the above discussion, we conclude that the observed EB effect in LiMn₂O₄ nanorods can be attributed to the coupling interaction at the interface between the AFM and cluster SG state.

In order to interpret figuratively the origin of the EB effect observed in LiMn₂O₄ nanorods, we propose a phenomenological model to illustrate the configurations of the coexistence

between the cluster SG state and AFM long-range order in this interesting EB system. When LiMn₂O₄ nanorods are cooled through $T_N \sim 60$ K with an applied magnetic field, the cluster SG-type freezing occurs simultaneously with the onset of AFM order. In this case, a configuration where SG clusters are embedded in an AFM matrix appears, which results in natural AFM/SG interfaces, as demonstrated in Fig. 12(a). The coupling interaction at the interfaces exerts an additional torque on the SG spins, which an extra magnetic field will be required to overcome. Thus, the hysteresis loop is shifted along the magnetic field axis, i.e., the EB effect arises. On the other hand, with decreasing temperature, more and more AFM superspins are frozen, and then a complete cluster SG phase forms when cooling to below T_f . However, not all eightfold ring clusters are in the frozen state, as was shown by Greedan *et al.*, that about half the spins of manganese ions are involved in long-range order and the other half are in a SG-like configuration at the ground state [12]. This spin configuration can be extended to the LiMn₂O₄ nanorods, which means that the long-range AFM order is not destroyed by the appearance of a cluster SG state. In this circumstance, the AFM clusters (eightfold ring clusters of Mn⁴⁺) are embedded in the SG matrix, as shown in Fig. 12(b). Likewise, the EB effect could be attributed to the coupling effect at the interface between the AFM and cluster SG states.

IV. CONCLUSIONS

In summary, single-crystalline LiMn₂O₄ nanorods have been synthesized via a simple solid-state reaction and characterized by various techniques. Magnetic measurements show that there exists a phase coexistence of the AFM long-range ordered phase due to eightfold rings of the Mn⁴⁺-Mn⁴⁺ interaction along with the cluster SG state originating from the freezing of large AFM clusters at low temperature in LiMn₂O₄ nanorods. The analysis of dynamical behavior of spins by means of the Vogel-Fulcher law and power law verifies the formation of the cluster SG state in LiMn₂O₄ nanorods. Furthermore, FC loops and TE measurements confirm the existence of an EB effect in the LiMn₂O₄ nanorods. By analyzing the TE data using Binek's model, we argue that the exchange coupling interaction at the interface between the AFM and cluster SG states leads to the observed EB effect in LiMn₂O₄ nanorods. A phenomenological model based on phase coexistence is proposed to interpret the origin of the EB effect in the present compound.

ACKNOWLEDGMENTS

We acknowledge the financial support from the Natural Science Foundation of China (No. 11364002, No. 11764004, No. 51302040, and No. 11547259) and the Science and Technology Project of Jiangxi Provincial Department of Education (GJJ14666).

[1] J. Lu, C. Zhan, T. Wu, J. Wen, Y. Lei, A. J. Kropf, H. Wu, D. J. Miller, J. W. Elam, Y. K. Sun, X. Qiu, and K. Amine, *Nat. Commun.* **5**, 5693 (2014).

[2] D. Alikin, A. Ievlev, S. Y. Luchkin, A. Turygin, V. Y. Shur, S. Kalinin, and A. Kholkin, *Appl. Phys. Lett.* **108**, 113106 (2016).

- [3] K. Suzuki, B. Barbiellini, Y. Orikasa, N. Go, H. Sakurai, S. Kaprzyk, M. Itou, K. Yamamoto, Y. Uchimoto, Y. J. Wang, H. Hafiz, A. Bansil, and Y. Sakurai, *Phys. Rev. Lett.* **114**, 087401 (2015).
- [4] M. Hirayama, H. Ido, K. Kim, W. Cho, K. Tamura, J. Mizuki, and R. Kanno, *J. Am. Chem. Soc.* **132**, 15268 (2010).
- [5] W. Tang, Y. Hou, F. Wang, L. Liu, Y. Wu, and K. Zhu, *Nano Lett.* **13**, 2036 (2013).
- [6] D. K. Kim, P. Muralidharan, H. W. Lee, R. Ruffo, Y. Yang, C. K. Chan, H. Peng, R. A. Huggins, and Y. Cui, *Nano Lett.* **8**, 3948 (2008).
- [7] S. Kim, M. Aykol, and C. Wolverton, *Phys. Rev. B* **92**, 115411 (2015).
- [8] J. J. Rodriguez-Carvajal, G. Rousse, C. Masquelier, and M. Hervieu, *Phys. Rev. Lett.* **81**, 4660 (1998).
- [9] S. Chowki, S. Rayaprol, and N. Mohapatra, *Mater. Res. Express* **1**, 046113 (2014).
- [10] V. W. J. Verhoeven, I. M. de Schepper, G. Nachttegaal, A. P. M. Kentgens, E. M. Kelder, J. Schoonman, and F. M. Mulder, *Phys. Rev. Lett.* **86**, 4314 (2001).
- [11] Y. Jang, F. Chou, and Y. M. Chiang, *Appl. Phys. Lett.* **74**, 2504 (1999).
- [12] J. E. Greedan, C. R. Wiebe, A. S. Wills, and J. R. Stewart, *Phys. Rev. B* **65**, 184424 (2002).
- [13] I. Tomeno, Y. Kasuya, and Y. Tsunoda, *Phys. Rev. B* **64**, 094422 (2001).
- [14] J. Gaddy, J. Lamsal, M. Petrovic, W. Montfrooij, A. Schmetz, and T. Vojta, *J. Appl. Phys.* **105**, 07D532 (2009).
- [15] J. Sugiyama, T. Hioki, S. Noda, and M. Kontani, *J. Phys. Soc. Jpn.* **66**, 1187 (1997).
- [16] Y. Oohara, J. Sugiyama, and M. Kontani, *J. Phys. Soc. Jpn.* **68**, 242 (1999).
- [17] S. Takano, T. Kaji, S. Okubo, H. Ohta, M. Yoshida, S. Kimura, R. Dziembaj, M. Molenda, C. Rudowicz, Y. Inagaki, and T. Asano, *J. Phys.: Condens. Matter* **19**, 145266 (2007).
- [18] S. Giri, A. Poddar, and T. Nath, *AIP Adv.* **1**, 032110 (2011).
- [19] V. Markovich, I. Fita, A. Wisniewski, D. Mogilyansky, R. Puzniak, L. Titelman, C. Martin, and G. Gorodetsky, *Phys. Rev. B* **81**, 094428 (2010).
- [20] M. Tadic, I. Milosevic, S. Kralj, M. L. Saboungi, and L. Motte, *Appl. Phys. Lett.* **106**, 183706 (2015).
- [21] M. J. Benitez, O. Petravic, E. L. Salabas, F. Radu, H. Tüysüz, F. Schüth, and H. Zabel, *Phys. Rev. Lett.* **101**, 097206 (2008).
- [22] T. Maity, S. Goswami, D. Bhattacharya, and S. Roy, *Phys. Rev. B* **89**, 140411 (2014).
- [23] X. Wang and Y. Li, *J. Am. Chem. Soc.* **124**, 2880 (2002).
- [24] A. Wills, N. Raju, and J. Greedan, *Chem. Mater.* **11**, 1510 (1999)..
- [25] T. Moriya, *Phys. Rev.* **120**, 91 (1960).
- [26] I. Dzyaloshinsky, *J. Phys. Chem. Solids* **4**, 241 (1958).
- [27] X. Huang, J. Ding, Z. Jiang, Y. Yin, Q. Yu, and X. Li, *J. Appl. Phys.* **106**, 083904 (2009).
- [28] J. de Almeida and D. J. Thouless, *J. Phys. A: Math. Gen.* **11**, 983 (1978).
- [29] S. Ghara, B. G. Jeon, K. Yoo, K. H. Kim, and A. Sundaresan, *Phys. Rev. B* **90**, 024413 (2014).
- [30] M. A. Girtu, C. M. Wynn, W. Fujita, K. Awaga, and A. J. Epstein, *Phys. Rev. B* **57**, 11058(R) (1998).
- [31] A. Ramirez, *Annu. Rev. Mater. Sci.* **24**, 453 (1994).
- [32] P. C. Hohenberg and B. I. Halperin, *Rev. Mod. Phys.* **49**, 435 (1977).
- [33] J. A. Mydosh, *Spin Glasses: An Experimental Introduction* (Taylor & Francis, London, 1993).
- [34] Q. Xu, S. Zhou, D. Wu, M. Uhlarz, Y. Tang, K. Potzger, M. Xu, and H. Schmidt, *J. Appl. Phys.* **107**, 093920 (2010).
- [35] V. K. Anand, D. T. Adroja, and A.D. Hillier, *Phys. Rev. B* **85**, 014418 (2012).
- [36] B. Maji, K. Suresh, and A. Nigam, *J. Phys.: Condens. Matter* **23**, 506002 (2011).
- [37] K. Binder and A. P. Young, *Phys. Rev. B* **29**, 2864 (1984).
- [38] T. Jonsson, P. Svedlindh, and M. F. Hansen, *Phys. Rev. Lett.* **81**, 3976 (1998).
- [39] M. D. Mukadam, S. M. Yusuf, P. Sharma, S. K. Kulshreshtha, and G. K. Dey, *Phys. Rev. B* **72**, 174408 (2005).
- [40] J. Lago, S. J. Blundell, A. Eguia, M. Jansen, and T. Rojo, *Phys. Rev. B* **86**, 064412 (2012).
- [41] A. Malinowski, V. L. Bezusyy, R. Minikayev, P. Dziawa, Y. Sryanyy, and M. Sawicki, *Phys. Rev. B* **84**, 024409 (2011).
- [42] S. Dong, Y. Yao, Y. Hou, Y. Liu, Y. Tang, and X. Li, *Nanotechnology* **22**, 385701 (2011).
- [43] S. Shtrikman and E. Wohlfarth, *Phys. Lett. A* **85**, 467 (1981).
- [44] J. L. Tholence, *Physica B+C* **126**, 157 (1984).
- [45] S. Mukherjee, R. Ranganathan, P. S. Anilkumar, and P. A. Joy, *Phys. Rev. B* **54**, 9267 (1996).
- [46] J. Souletie and J. L. Tholence, *Phys. Rev. B* **32**, 516 (1985).
- [47] P. M. Shand, A. L. Meyer, M. Streicher, A. Wilson, T. Rash, M. W. Roth, T. E. Kidd, and L. H. Strauss, *Phys. Rev. B* **85**, 144432 (2012).
- [48] H. G. Schimmel, W. Montfrooij, G. J. Kearley, V. W. J. Verhoeven, and I. M. de Schepper, *Phys. Rev. B* **63**, 214409 (2001).
- [49] P.-z. Wong, S. von Molnar, T. T. M. Palstra, J. A. Mydosh, H. Yoshizawa, S. M. Shapiro, and A. Ito, *Phys. Rev. Lett.* **55**, 2043 (1985).
- [50] H. Yoshizawa, S. Mitsuda, H. Aruga, and A. Ito, *Phys. Rev. Lett.* **59**, 2364 (1987).
- [51] S. Chillal, M. Thede, F. J. Litterst, S. N. Gvasaliya, T. A. Shaplygina, S. G. Lushnikov, and A. Zheludev, *Phys. Rev. B* **87**, 220403 (2013).
- [52] W. Kleemann, V. V. Shvartsman, P. Borisov, and A. Kania, *Phys. Rev. Lett.* **105**, 257202 (2010).
- [53] S. Giri, M. Patra, and S. Majumdar, *J. Phys.: Condens. Matter* **23**, 073201 (2011).
- [54] J. Nogués, J. Sort, V. Langlais, V. Skumryev, S. Surinach, J. Munoz, and M. Baró, *Phys. Rep.* **422**, 65 (2005).
- [55] T. Maity, S. Goswami, D. Bhattacharya, and S. Roy, *Phys. Rev. Lett.* **110**, 107201 (2013).
- [56] T. Maity, S. Goswami, D. Bhattacharya, and S. Roy, *Phys. Rev. Lett.* **114**, 099704 (2015).
- [57] B. M. Wang, Y. Liu, P. Ren, B. Xia, K. B. Ruan, J. B. Yi, J. Ding, X. G. Li, and L. Wang, *Phys. Rev. Lett.* **106**, 077203 (2011).
- [58] S. N. Jammalamadaka, S. Rao, S. Bhat, J. Vanacken, and V. Moshchalkov, *AIP Adv.* **2**, 012169 (2012).
- [59] S. Karmakar, S. Taran, E. Bose, B. K. Chaudhuri, C. P. Sun, C. L. Huang, and H. D. Yang, *Phys. Rev. B* **77**, 144409 (2008).
- [60] J. Geshev, *J. Appl. Phys.* **105**, 066108 (2009).
- [61] J. Geshev, *J. Phys.: Condens. Matter* **21**, 078001 (2009).

- [62] I. Fita, A. Wisniewski, R. Puzniak, P. Iwanowski, V. Markovich, S. Kolesnik, and B. Dabrowski, *Phys. Rev. B* **95**, 134428 (2017).
- [63] M. R. Fitzsimmons, C. Dufour, K. Dumesnil, J. Dou, and M. Pechan, *Phys. Rev. B* **79**, 144425 (2009).
- [64] P. K. Manna, S. M. Yusuf, R. Shukla, and A. K. Tyagi, *Phys. Rev. B* **83**, 184412 (2011).
- [65] R. P. Singh and C. Tomy, *Solid State Commun.* **150**, 804 (2010).
- [66] N. Moutis, C. Christides, I. Panagiotopoulos, and D. Niarchos, *Phys. Rev. B* **64**, 094429 (2001).
- [67] X. H. Huang, J. F. Ding, G. Q. Zhang, Y. Hou, Y. P. Yao, and X. G. Li, *Phys. Rev. B* **78**, 224408 (2008).
- [68] J. F. Ding, O. I. Lebedev, S. Turner, Y. F. Tian, W. J. Hu, J. W. Seo, C. Panagopoulos, W. Prellier, G. Van Tendeloo, and T. Wu, *Phys. Rev. B* **87**, 054428 (2013).
- [69] M. Vafaei, S. Finizio, H. Deniz, D. Hesse, H. Zabel, G. Jakob, and M. Kläui, *Appl. Phys. Lett.* **108**, 072401 (2016).
- [70] S. Mukherjee, W. Kreuzpaintner, J. Stahn, J. G. Zheng, A. Bauer, P. Böni, and A. Paul, *Phys. Rev. B* **91**, 104419 (2015).
- [71] D. Paccard, C. Schlenker, O. Massenet, R. Montmory, and A. Yelon, *Phys. Status Solidi* **16**, 301 (1966).
- [72] T. Hauet, J. A. Borchers, P. Mangin, Y. Henry, and S. Mangin, *Phys. Rev. Lett.* **96**, 067207 (2006).
- [73] A. Hoffmann, *Phys. Rev. Lett.* **93**, 097203 (2004).
- [74] S. R. Ali, M. R. Ghadimi, M. Fecioru-Morariu, B. Beschoten, and G. Güntherodt, *Phys. Rev. B* **85**, 012404 (2012).
- [75] C. Binek, *Phys. Rev. B* **70**, 014421 (2004).
- [76] Y. K. Tang, Y. Sun, and Z. H. Cheng, *Phys. Rev. B* **73**, 174419 (2006).